Bubble Dynamics in a 3-D Gas–Solid Fluidized Bed Using Ultrafast Electron Beam X-Ray Tomography and Two-Fluid Model

Vikrant Verma, Johan T. Padding, Niels G. Deen, and J. A. M. (Hans) Kuipers
Dept. of Chemical Engineering and Chemistry, Eindhoven University of Technology, 5600 MB Eindhoven, The Netherlands

Frank Barthel
Institute of Fluid dynamics, Helmholtz-Zentrum Dresden-Rossendorf Bautzner Landstr. 400, 01328 Dresden, Germany

Martina Bieberle, Michael Wagner, and Uwe Hampel
Institute of Fluid dynamics, Helmholtz-Zentrum Dresden-Rossendorf Bautzner Landstr. 400, 01328 Dresden, Germany

AREVA Endowed Chair of Imaging Techniques in Energy and Process Engineering, Technische Universitaet Dresden, 01062 Dresden, Germany

DOI 10.1002/aic.14393
Published online February 14, 2014 in Wiley Online Library (wileyonlinelibrary.com)

Bubble characteristics in a three-dimension gas-fluidized bed (FB) have been measured using noninvasive ultrafast electron beam X-ray tomography. The measurements are compared with predictions by a two-fluid model (TFM) based on kinetic theory of granular flow. The effect of bed material (glass, alumina, and low linear density polyethylene (LLDPE), d_p ~1 mm), inlet gas velocity, and initial particle bed height on the bubble behavior is investigated in a cylindrical column of 0.1-m diameter. The bubble rise velocity is determined by cross correlation of images from dual horizontal planes. The bubble characteristics depend highly upon the particle collisional properties. The bubble sizes obtained from experiments and simulations show good agreement. The LLDPE particles show high gas hold-up and higher bubble rise velocity than predicted on basis of literature correlations. The bed expansion is relatively high for LLDPE particles. The X-ray tomography and TFM results provide in-depth understanding of bubble behavior in FBs containing different granular material types. © 2014 American Institute of Chemical Engineers *AIChE J*, 60: 1632–1644, 2014
Keywords: fluidized bed, X-ray tomography, two-fluid model, bubbles

Introduction

Gas-fluidized beds (FBs) are used extensively in process industries because of their excellent mixing, heat and mass transfer characteristics. They are currently used in separation, classification, drying and mixing of particles, chemical reactions, and regeneration processes.[1] The performance of a FB is majorly governed by the formation of gas bubbles and their distribution, facilitating rapid solids mixing, and high heat transfer rates to immersed surfaces. Therefore, understanding of the formation and propagation of gas bubbles is the key to scale-up of gas–solid FB reactors. Conversely, lack of understanding of the fundamentals of dense gas-particle flows in general has led to several difficulties in the design and scale-up of these reactors.[2] Although computational fluid dynamics (CFD) tools are more and more used to gain a detailed understanding of flow structures inside the FBs, validation of such simulation models using advanced and detailed experiments is crucial. Unfortunately, due to the opaqueness of FBs, flow visualization and measurements are difficult to perform. Earlier invasive probes were used for measurements in FBs,[3,4] with the obvious limitation of altering the flow structure in their surroundings.[5] Noninvasive measurement techniques are therefore preferred. Various tomographic imaging techniques have been developed for multiphase flow measurements,[5–7] including electrical impedance tomography, electrical resistance tomography, electrical capacitance tomography (ECT), ultrasonic computed tomography, computed tomography densitometry, X-ray computed tomography, positron emission tomography, neutron emission tomography, and magnetic resonance imaging. Among these, ECT is widely used to study local gas and solid distribution inside the FBs due to the inexpensive and easy handling of the technique.[8,9] In ECT, the number of independent capacitors is usually limited, leading to an underdetermined problem for reconstruction of the tomographic images. These images are, therefore, highly sensitive with respect to the choice of reconstruction algorithm. Also, due to its relatively poor resolution, ECT fails to resolve

Correspondence concerning this article should be addressed to J. T. Padding at j.t.padding@tue.nl.

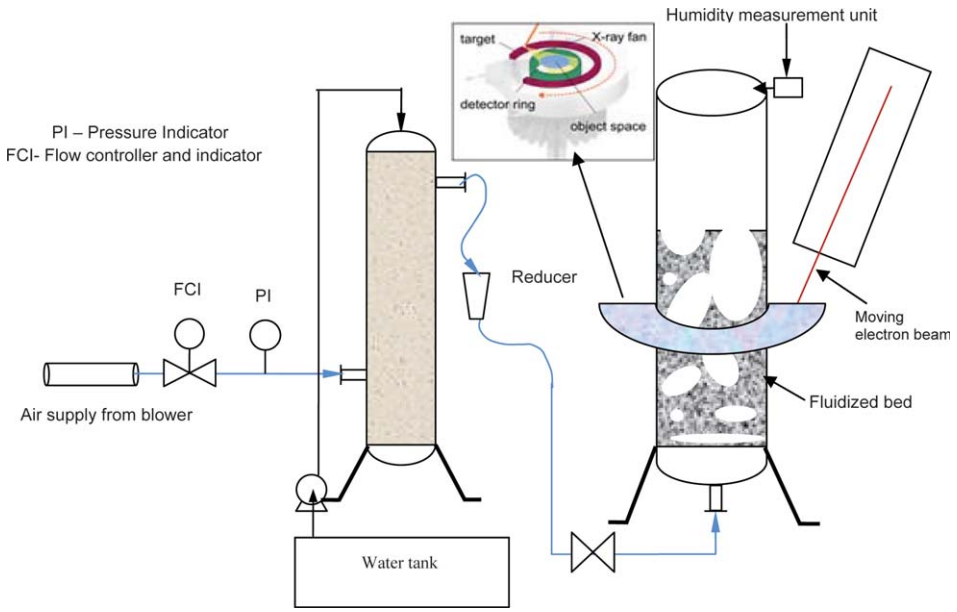

Figure 1. Schematic representation of the experimental X-ray tomography setup for FB system.

[Color figure can be viewed in the online issue, which is available at wileyonlinelibrary.com.]

the flow structure inside dense beds.[8] X-ray tomography techniques can achieve much higher resolution and are gaining more attention in the research for flow visualization. It can provide planar solid distribution profiles in a FB without disturbing the internal flow. The X-ray system needs to be very fast to acquire high temporal and spatial resolution data in a FB. Researchers[10] studied bubble characteristics and gas holdup, respectively, using X-ray fluoroscopy techniques. Recently, Bieberle et al.[11] and Brouwer et al.[12] showed the large potential of the X-ray tomographic technique to study gas–solids flow. The ultrafast electron beam X-ray tomography technique developed by Hampel and coworkers is emerging as a powerful technique, which can provide high temporal (up to 7000 fps) and spatial ($\sim$1 mm) resolution.[13,14].

In this article, we take advantage of the combined availability of modern X-ray facilities, computational power, and sophisticated CFD algorithms to make a one-to-one comparison between experiments and simulations of a three-dimension (3-D) cylindrical gas FB. This will allow us to gain detailed understanding of the flow structure. At the same time, this will allow us to validate the CFD models. The ultrafast electron beam X-ray scanner, developed at Helmholtz-Zentrum Dresden-Rossendorf, was used for the experimental measurements. Simulations were performed using the two-fluid model (TFM) based on the kinetic theory of granular flow (KTGF). In this model, the gas and solid phases are treated as interpenetrating continua, where the KTGF is used to provide closures for representation of the particle–particle interactions. Although the TFM has been extensively used and validated in the open literature[15–19] this has been mainly done for two-dimension (2-D) systems. A detailed 3-D validation was lacking until now. So far, the flow characteristics obtained for 3-D FBs were mostly compared with 2-D or axis-symmetric simulations,[20] but the validity of these simulations can be questioned. As Geldart[21] reported, in a 2-D bed bubbles are restrained by the walls in one-dimension, becoming slugs when viewed from the side of the bed, contributing to a greater bed expansion and leading to considerable differences in particle and bubble characteristics. Chandrasekaran et al.[22] report a combined experimental and simulation study of a 3-D FB for low linear density polyethylene (LLDPE) particles on a very coarse grid simulation using MFIX. To the best of our knowledge, no any other detailed parametric combined experimental and simulation study has been reported in the literature.

In this work, we report on experimental and simulation investigations of a 0.1-m diameter cylindrical FB. The X-ray scanner performs dual plane measurements, where two cross-sectional planes, separated by 11-mm vertical distance, are measured simultaneously. Dual plane measurements allow us to investigate the cross-correlation between the two planes to obtain the bubble rise velocity. Measurements have been performed at different heights from the bottom of the gas distributor. A highly efficient TFM for 3-D cylindrical geometries, presented in Verma et al.[23] has been used for the simulations. We study the effect of different granular material types, different superficial gas velocities, and different bed aspect ratios on bubble characteristics such as bubble size, bubble velocity, bubble size distribution, and porosity distribution. To make a fair comparison, we use nearly identical postprocessing approaches to both the experimental and simulation data.

This article is organized as follows. We first provide the essential details of the experimental setup, the TFM model, and postprocessing of the data, respectively, followed by results and discussion and finally our conclusions.

Experimental Setup

A schematic representation of the experimental setup is shown in Figure 1. A cylindrical column made of a polycarbonate tube with inner diameter of 0.1 m and height of 1.4 m was used. This dimension of the column has been chosen due to space limitations in the X-ray scanner, which can scan a column of maximum diameter 12 cm. Details of the ultrafast electron beam X-ray scanner have been reported by Fischer and Hampel.[24] A 25-mA beam current was used to produce X-rays at a circular metal target. Because of the fast

Table 1. TFM Governing Equations

Continuity equation: (T1-1)

$$\frac{\partial(\varepsilon_g\rho_g)}{\partial t}+\nabla\cdot\left(\varepsilon_g\rho_g\bar{u}_g\right)=0$$

$$\frac{\partial(\varepsilon_s\rho_s)}{\partial t}+\nabla\cdot\left(\varepsilon_s\rho_s\bar{u}_s\right)=0$$

Momentum equation: (T1–2)

$$\frac{\partial(\varepsilon_g\rho_g\bar{u}_g)}{\partial t}+\nabla\cdot\left(\varepsilon_g\rho_g\bar{u}_g\bar{u}_g\right)=-\varepsilon_g\nabla p_g-\nabla\cdot\left(\varepsilon_g\bar{\bar{\tau}}_g\right)-\beta\left(\bar{u}_g-\bar{u}_s\right)+\varepsilon_g\rho_g\bar{g}$$

$$\frac{\partial(\varepsilon_s\rho_s\bar{u}_s)}{\partial t}+\nabla\cdot\left(\varepsilon_s\rho_s\bar{u}_s\bar{u}_s\right)=-\varepsilon_s\nabla p_g-\nabla p_s-\nabla\cdot\left(\varepsilon_s\bar{\bar{\tau}}_s\right)+\beta\left(\bar{u}_g-\bar{u}_s\right)+\varepsilon_s\rho_s\bar{g}$$

Granular temperature equation: (T1–3)

$$\frac{3}{2}\left[\frac{\partial}{\partial t}\left(\varepsilon_s\rho_s\Theta\right)+\ \nabla\cdot\left(\varepsilon_s\rho_s\Theta\bar{u}_s\right)\right]=-\left(p_s\bar{\bar{I}}+\varepsilon_s\bar{\bar{\tau}}_s\right):\nabla\bar{u}_s-\nabla\cdot\left(\varepsilon_s q_s\right)-3\beta\Theta-\gamma$$

operation of the X-ray scanner, the image processing is done offline after the measurements. The raw images obtained from the measurement were reconstructed with the help of in-house developed reconstruction software using a filtered back projection method. In this work, dual plane measurements were performed for a total duration of 20 s at an expected spatial resolution of 1 mm, and a temporal resolution of 1000 cross-sectional images per second. In total, 20,000 images were obtained for each plane in a single measurement. These images have a format of 128 × 128 pixels, with each pixel size approximately 0.78 mm. Each pixel value represents the local linear X-ray attenuation, correlating with local material density. This results in differences in gray-level in the images for the gas and solid phases in FBs. Spherical LLDPE particles, alumina particles, and glass particles were used for this investigation, where all diameters were in the approximate range of 1 mm. LLDPE and alumina particles of this size can definitely be classified as Geldart B type particles, whereas the glass particles lie on the border between Geldart B and D classification. The choice of these materials has been made on the basis of difference in attenuation of X-rays. Glass particles, with a higher density, exhibit more attenuation compared to LLDPE and alumina particles. The particles also differ in their collisional properties, with nearly ideal glass particle collisions, and alumina and LLDPE particles prevailing toward nonideal collisions. Measurements were performed for (static) bed aspect ratios of 0.5 (measurement height 5 cm), 1.0 (measurement height 5 and 10 cm), and 2.0 (measurement height 5, 10, and 20 cm). Four superficial gas velocities of $1.25U_{mf}$, $1.50U_{mf}$, $2.0U_{mf}$, and $3.0U_{mf}$ have been studied, except for glass for which $3.0U_{mf}$ was not considered. Experiments were conducted at ambient conditions with air as fluidizing medium. Pressurized air was fed through the bottom of the column. The air was supplied by a two stage side channel blower, with a maximum capacity of 205 m^3/h, and a power of 4 kW. The air flow rate was controlled by a frequency controller. To prevent any electrostatic charge buildup during fluidization, the air was passed through a humidifier before it was led to the FB. Despite this, the LLDPE particles still exhibited electrostatic charging with the internal walls of the column. Therefore, the internal wall was partly covered with very thin aluminum tape grounded to the earth, to prevent electrostatic wall effects.

Two-fluid Model

The two-fluid continuum model describes both the gas phase and the solids phase as fully interpenetrating continua using a generalized form of the Navier–Stokes equations.[25,26] To describe the solids phase, the KTGF[27,28] is used. The conservation equations are given in Tables 1 and 2. Here, the subscripts "g" and "s" represent the gas and solids phase, respectively. The numerical method that we use to solve the governing equations is based on a finite difference technique. The pressure gradients and viscous terms have been discretized by standard central differencing, whereas the convection terms have been evaluated by a deferred correction using a

Table 2. KTGF Closures for TFM

Particle pressure: (T2-1)

$$p_s=\ [1+2(1+e_n)\varepsilon_s g_0]\varepsilon_s\rho_s\Theta$$

Bulk viscosity: (T2-2)

$$\lambda_s=\frac{4}{3}\varepsilon_s\rho_s d_p g_o(1+e_n)\sqrt{\frac{\Theta}{\pi}}$$

Shear viscosity: (T2–3)

$$\mu_s=1.01600\frac{5}{96}\pi\rho_s d_p\sqrt{\frac{\Theta}{\pi}}\frac{(1+\frac{8}{5}\frac{(1+e_n)}{2}\varepsilon_s g_0)(1+\frac{8}{5}\varepsilon_s g_0)}{\varepsilon_s g_0}+\frac{4}{5}\varepsilon_s\rho_s d_p g_0(1+e_n)\sqrt{\frac{\Theta}{\pi}}$$

Dissipation of granular energy due to inelastic particle–particle collision: (T2–4)

$$\gamma=3\left(1-e_n^2\right)\varepsilon_s^2\rho_s g_0\Theta\left[\frac{4}{d_p}\sqrt{\frac{\Theta}{\pi}}-(\nabla\cdot\bar{u}_s)\right]$$

Pseudo-Fourier fluctuating kinetic energy flux: $\bar{q}_s=-\kappa_s\nabla\Theta$ (T2–5)

Pseudo thermal conductivity: (T2–6)

$$\kappa_s=1.02513\frac{75}{384}\pi\rho_s d_p\sqrt{\frac{\Theta}{\pi}}\frac{(1+\frac{12}{5}\frac{(1+e_n)}{2}\varepsilon_s g_0)(1+\frac{12}{5}\varepsilon_s g_0)}{\varepsilon_s g_0}+2\varepsilon_s\rho_s d_p g_0(1+e_n)\sqrt{\frac{\Theta}{\pi}}$$

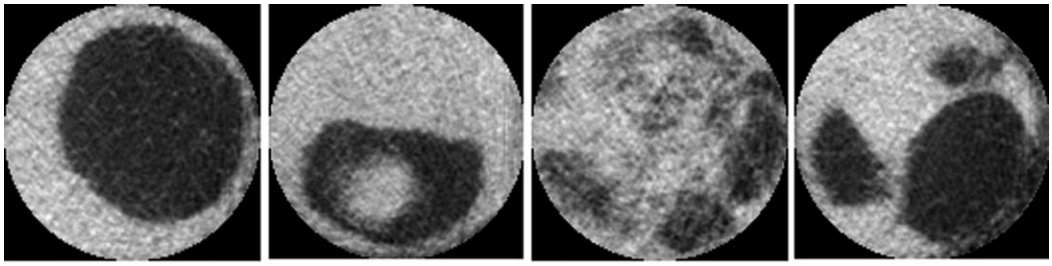

Figure 2. Examples of different bubble shapes observed experimentally in cross-sectional planes during fluidization.

(a) spherical bubbles, (b) arcs (wakes), (c) irregular bubbles, and (d) splitting bubbles.

total variation diminishing scheme. The normal derivatives of the viscous terms and the upwind part of the convection term have been treated in an implicit manner to improve stability and reduce calculation time. For more details on the actual discretization and implementation, the reader is referred to Ref. 23. In this work, the gas-particle drag force correlation developed by Van der Hoef et al.[29] has been used. In regions of dense solid packing, friction stresses for the solids phase have been used, as described in Ref. 30.

Postprocessing

As already mentioned, different gray-levels in the X-ray images distinguish the solids and gas phase. As the spatial resolution is approximately in the range of a single particle size, individual particles are not easy to distinguish. However, gas bubbles are easily captured due to the different local attenuation of X-rays in the emulsion and gas phase. High and low contrast in the images is associated with high and low density of particles, respectively, where glass particles (high density) show higher contrast and LLDPE particles (low density) show lower contrast. Selected reconstructed images are shown in Figure 2. This figure clearly shows the range of different detected bubble shapes, from regular to irregular.

Bubble size

Experiments. The reconstructed images (as shown in Figure 2) were used to detect and calculate the size of the bubbles. The image processing tool box of MATLAB was used to calculate the equivalent bubble diameter from individual images. The different steps for image processing included: (a) removing noise and enhancing the contrast for low contrast images; (b) binarizing image data, with a threshold level detected from individual images using the Otsu method[31]; (c) extracting the circular region of interest (square images were obtained from the measurements); (d) applying an edge detection method to detect sharp bubble boundaries in the binary image; (e) smoothening of the bubble boundary, deleting particle shade, and very small voids near the bubble boundary; (f) calculating the detected bubble area, and the effective bubble diameter from this area using Eq. 1. The number of bubbles detected was used to obtain the number averaged bubble diameter, the so-called equivalent bubble diameter (from Eq. 2) at each measurement height

$$D_{b,i} = \sqrt{\frac{4A_b}{\pi}} \tag{1}$$

$$D_e = \frac{1}{N_b}\sum_{i=1}^{N_b} D_{b,i} \tag{2}$$

Simulations. Very similar steps as used in the experiments were involved in calculating the equivalent bubble diameter from the simulation data. The simulations provide porosity values in each computational cell. These porosity values are used to define bubbles. The threshold value to define bubble in the simulations plays an important role. To calculate an accurate threshold value from simulations, the Otsu method[31] used in step (b) above has been used here as well. Testing different sets of data, the best choice for the threshold value turns out to be a porosity value of 0.7. Indeed, visualization of porosity plots revealed that a porosity greater than 0.7 should be attributed to a bubble. A linear interpolation technique was used to calculate the precise subgrid position of the boundary in the sharp gradient between bubble and emulsion phase. Number averaging is performed to obtain the equivalent bubble diameter.

The measured and the predicted equivalent bubble diameters are compared with the correlations of Darton et al.[32] and Werther.[33] Expressions for these correlations are given in Table 3.

Cross-correlation function

The dual plane measurements allow us to calculate cross correlations between the signals from two planes, separated

Table 3. Equivalent Bubble Size Correlations Compared in this Work

Author(s)	Correlation	$U_0 - U_{mf}$ (m/s)	Bed Size (m)
Darton et al.[32]	$D_e = 0.54(U_0 - U_{mf})^{0.4}\left(H + 4\sqrt{A_0}\right)^{0.8} g^{-0.2}$	0.005–0.2	0.3 × 0.3 0.3 × 0.2 0.61 × 0.61 1.0
Werther[33]	$D_e = d_0[1 + 27(U_0 - U_{mf})]^{1/3}(1 + 6.4\mathrm{H})^{1.21}$	0.05–0.3	0.45 1.0
		Geldart A, $d_0 = 0.00620$ m Geldart B, $d_0 = 0.00853$ m Geldart D, $d_0 = 0.0123$ m	

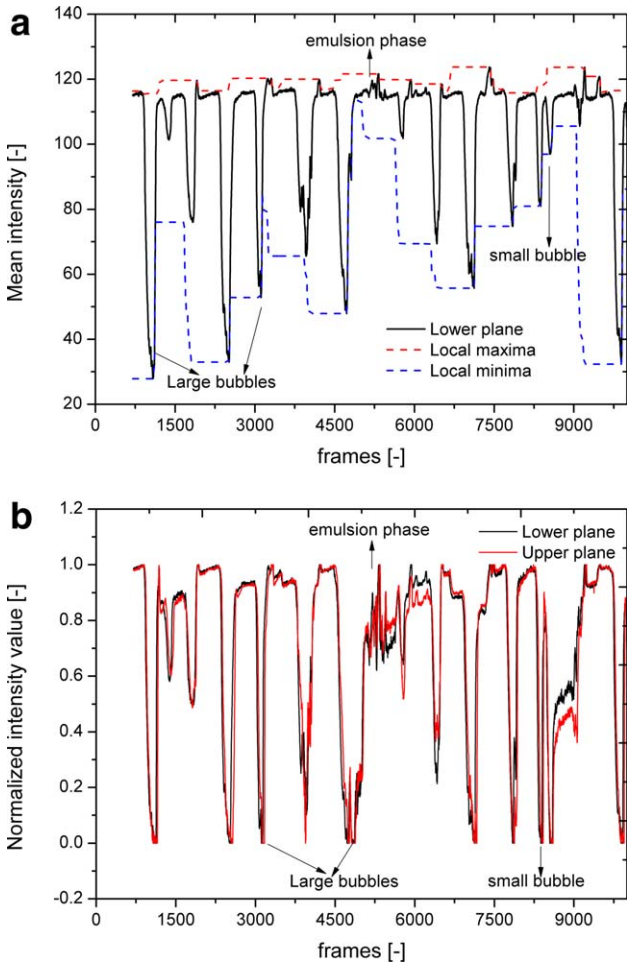

Figure 3. Example data of intensity plot of tomographic images.

(a) Mean intensity plot against time. (b) Normalized intensity plot against time. [Color figure can be viewed in the online issue, which is available at wileyonlinelibrary.com.]

by a vertical distance of 11 mm. A bubble rising in a FB will first cross the lower measurement plane, and some time later the upper measurement plane. This rapid event creates a phase shift in the top plane compared to the bottom plane, representing the time delay between the two signals and attributed to the bubble passage. The phase shift can be determined with a cross-correlation function (CCF). This function seeks the best overlapping fit of the two functions by shifting one in time. Figure 3a shows the mean intensity plot of the original images, where a lower value represents the occurrence of a bubble. The differences in height and width of the peaks clearly represent differences in bubble characteristics, where stronger signals represent larger bubbles and weaker signals smaller bubbles. As a consequence, when cross correlating these signals, bubbles get different weighted on different scales. This may lead to a signal that is biased toward larger bubbles and correspondingly toward the larger bubble velocities. Therefore, weak and strong signals should first be filtered to weigh them equally. This can be performed by normalizing the pixel intensity value between 0 and 1 with local maxima and local minima from Eq. 3. Local maxima and minima ($I_{\min}$ and $I_{\max}$) in Eq. 3 can be obtained in the neighborhood of each peak, with a choice of filter length of approximately 500–700 frames. This choice has to be made so that at least a pair of smaller and larger bubbles peaks lies in the same filter length. For example, the dashed line in Figure 3a that encloses the solid line represents the local maxima (red) and the local minima (blue). Figure 3b shows the same signal as in 3a, but small and large bubbles peaks are approximately on the same scale now. Thus, preprocessing of the signal is performed to obtain a normalized intensity before calculating the CCF

$$I_{\text{norm}} = \frac{I - I_{\min}}{I_{\max} - I_{\min}} \tag{3}$$

In our work, we applied a CCF for each individual pixel using the normalized intensity value. The individual pixel correlation allows us to find the spatial time delay (Eq. 4) as well as averaging it for the whole cross-sectional plane (Eq. 5) to find the average time delay. Once the time delay is calculated from the number of shifted frames, the bubble rise velocity can be obtained from Eq. 6

$$R(n,p) = \frac{1}{N_t} \sum_{i=1}^{N_t - n} I_{1,\text{norm}}(p,i) \cdot I_{2,\text{norm}}(p, i+n) \tag{4}$$

$$\bar{R}(n) = \frac{1}{N_{tp}} \sum_{i}^{N_{tp}} R(n,p) \tag{5}$$

$$\bar{V}_b = \frac{f \Delta z}{n_D} \tag{6}$$

In Eq. 4, $I_{1,\text{norm}}$ and $I_{2,\text{norm}}$ are the normalized intensity of a pixel in the lower and upper frame, respectively, at the location (pixel number) p. N_t is the total number of frames and N_{tp} is the total number of pixel in the cross-section measurement area. The index i indicates a frame number, and n is the number of frames over which the function is shifted. The CCF (Eq. 5) shows a maximum for a certain value of n, which we denote as n_D. The measured shift value n_D can be used to calculate the average bubble velocity ($\bar{V}_b$), given vertical distance ($\Delta z = 11$ mm) and measurement frequency ($f = 1000$ fps). Figure 4 shows an example of the CCF, showing a peak at $n_D = 24$ frames, corresponding to a time shift of 0.024 s and bubble velocity of 0.46 m/s.

To make a one-to-one comparison, a similar CCF has been determined in the simulation data, where the porosity

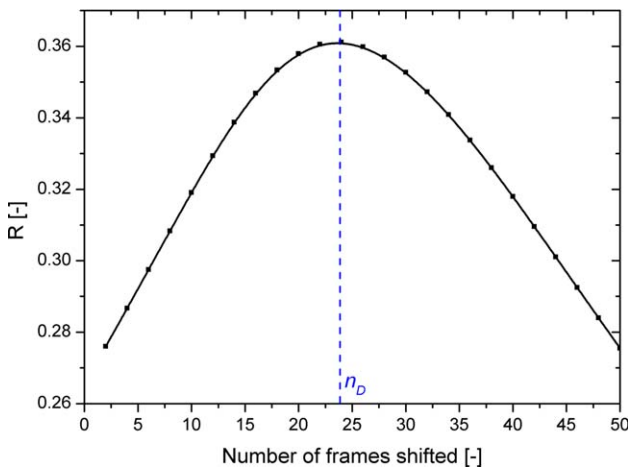

Figure 4. Example of normalized intensity CCF obtained from experiments.

The peak value at n_D is a measure for the average bubble rise velocity. [Color figure can be viewed in the online issue, which is available at wileyonlinelibrary.com.]

Table 4. Literature Correlation for Bubble Velocity for Geldart B Type Particles

Author(s)	Correlation	$U_0 - U_{mf}$ (m/s)	Bed Size (m)
Hilligardt and Werther[34]	$u_b = 0.2\sqrt{D}\,0.71\sqrt{g D_e} + \psi(U_0 - U_{mf})$	0.05–0.3	0.3 × 2.0
	$\psi = \begin{cases} 0.67 & \text{AR} < 1.7 \\ 0.51\sqrt{\text{AR}} & 1.7 \le \text{AR} \le 4 \\ 1 & \text{AR} > 4 \end{cases}$		0.5 × 0.5 1.0 × 1.0

values were weighted by the area of the cells. This is necessary because the area of a computational cell varies from the central axis to the circumference of the cylinder (using a cylindrical coordinate system). So Eq. 4 is rewritten as

$$R(n,p) = \frac{1}{N_t} \sum_{i=1}^{N_t - n} A_p \cdot \varepsilon_{g,1}(p,i) \cdot \varepsilon_{g,2}(p,i+n) \tag{7}$$

where ε_g is the local porosity (gas fraction) and A_p is the area of cell p. When averaging over all cells, we again apply Eq. 5 with N_{tp} equal to the total cross-sectional area. The vertical distance between two measurement planes in the simulations was 10 mm (five grid cells). A spline method was used to find an accurate correlation peak position in between integer frame numbers.

The measured and the predicted bubble velocities are compared with the correlation of Hilligardt and Werther.[34] The expression for their correlation is given in Table 4.

Porosity distribution

The porosity distribution function (PDF) quantifies the relative occurrence of porosities in the emulsion phase and the bubble phase. To obtain the PDF from the experimental results, the first step is to convert intensity values of the images into porosity. For this a random maximum packing of the bed is assumed, with a linear relation between porosity and normalized intensity values

$$\varepsilon_g = 1 - 0.64356 I_{norm} \tag{8}$$

Here, I_{norm} is given by Eq. 3, where in this case I_{min} and I_{max} are the minimum and maximum intensity values of the entire measurement series. These values are obtained from hand-selected images of the measurement series, which have clear large bubbles and a clear dense emulsion phase. The selection ensures that the correct minimum and maximum intensity is obtained from the measurement, which is especially important if the contrast of the images is low, such as for low density particles. The final step involves the construction of a histogram of all pixels over all time steps. We choose a relatively small porosity bin size of 0.04, which is why a sufficient number of images are required to obtain a smooth distribution. For the simulation results, the PDF was constructed from the final step using porosity values, again taking into account the variable cell size.

Table 5. Simulations and Experimental Setting

	Property Simulations	Values Experiments	Units
Radial length (cells)	0.05 (32)	0.05 (-)	m
Azimuthal angle (cells)	2π (32)	2π (-)	radian
Net height of the column (cells)	0.36 (180)	1.4 (-)	m
Particle bed height (AR = 0.5)	0.05	0.05	m
Particle bed height (AR = 1.0)	0.10	0.10	m
Particle bed height (AR = 2.0)	0.20	0.20	m
Time step	10^{-4}	–	s
Total time	20	20	s
Size of pores in gas distributor	–	0.7	mm

Results and Discussion

We will now investigate the effects of bed material, superficial inlet gas velocity, and bed aspect ratio on bubble characteristics such as bubble size, bubble distribution, porosity distribution, and bubble velocity. The experimental and simulation settings are presented in Table 5. Details of the particles are given in Table 6. For the comparison with experiments, the initial 1 s of the simulation data have been discarded to exclude startup effects from our measurements.

Bubble size distribution

Different bubble shapes were detected, ranging from approximately spherical to very irregular shapes (see Figure 2). Coalescence and breakup was observed in the image sequences as well as in the simulations. Chaotic motion of bubbles was observed both in the experiments and the simulations, as can be seen from the contour plots in Figures 5 and 6. Figure 5 shows the shape of bubbles reconstructed from pixel intensity values with time, where the vertical axis represents a bubble passage for a total time of 1 s. Note that the vertical axis cannot be transformed unambiguously to a length scale because different sized bubbles have different velocities. A noticeable difference could be observed between bubbles in the lower and upper plane. The actual shape and size of the bubbles can be obtained from the simulation contours shown in Figure 6. This figure shows that small bubbles emerge near the column wall and move toward the center due to a lower resistance in the center, leading to the formation of larger bubbles. All these observations are in good agreement with the theory of Kunii and Levelspiel.[1]

It is interesting to compute the bubble size distribution at different heights and for different inlet gas velocities.

Table 6. Particle Properties

Type	Density (kg/m^3)	Diameter (mm)		U_{mf} (m/s)	e_n (-)
		Simulations	Experiments	Sim./Exp.	
LLDPE	800	1.1	1.0 ± 0.3	0.26/0.24	0.69
Alumina	1040	1.0	1.0 ± 0.05	0.33/0.32	0.74
Glass	2526	1.0	1.0 ± 0.05	0.68/0.67	0.86

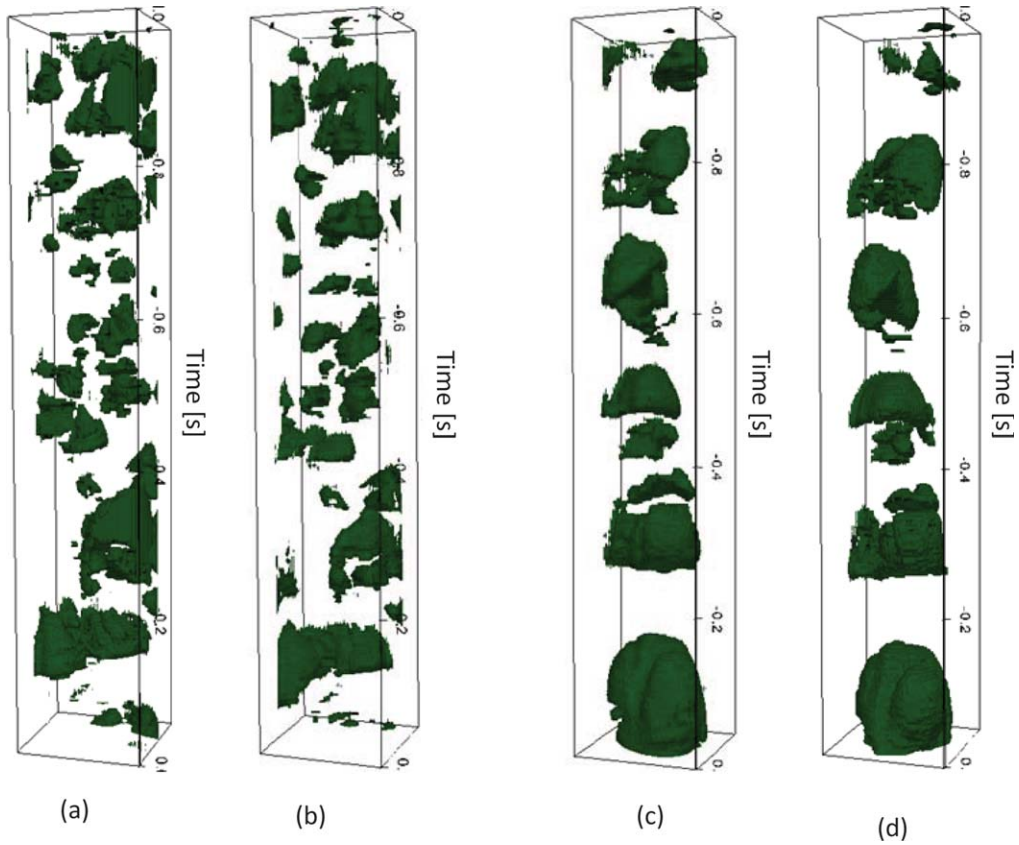

Figure 5. Quasi 3-D bubble shape reconstructed from tomographic images at 3.0 U_{mf} for LLDPE particles at a height of (a) 39 mm, (b) 50 mm, (c) 89 mm, and (d) 100 mm.

Pairs of image (a) and (b) are from the same measurement series obtained from lower and upper plane, respectively. Similarly for (c) and (d). [Color figure can be viewed in the online issue, which is available at wileyonlinelibrary.com.]

According to the two-phase theory of FBs,[35,36] a gas velocity above the minimum fluidization velocity U_{mf} contributes to bubble formation. Therefore, at a constant inlet gas velocity higher than U_{mf}, bubbles are formed and grow in size predominantly due to coalescence of small bubbles. This is confirmed in Figure 7, where at a height of 10 cm, a significant number of small bubbles and fewer larger bubbles are predicted, whereas at a height of 20 cm, the number of smaller bubbles decreases and the number of larger bubbles increases significantly. Figure 8 shows that with an increase in inlet gas velocity, the occurrence of larger bubbles increases, which is a well-known fact from two-phase theory. We note that in Figure 8 the simulations predict many smaller bubbles compared to experimental observations. A detailed discussion on this behavior will be presented in a later part of this article, when we compare bubble sizes from experiments and simulations.

The PDF plot of the porosity in Figure 9 shows a bubble peak (porosity close to 1), which increases with increased height due to the higher volume fraction of gas present in the top section of the bed. Figure 9 also reveals that with increasing height, the emulsion phase gets denser, that is, bubbles are extracting gas from the emulsion phase. This reveals that the bubble size does not only increase due to coalescence but also due to extraction of gas by the bubble from the surrounding emulsion phase. Please note that in each of the PDF Figures 9, 10, and 12, graphs of different color correspond to independent measurement series, which may have different contrast in the X-ray images. However, the height and width of the bubble peak and the dense emulsion peak can be compared.

The gas extraction process for different materials can be compared from pairs of measurements in Figures 10 and 12. Figure 10 shows that, irrespective of the relatively lower excess gas velocity for LLDPE particles, the high porosity regions (bubbles) appear more frequently for the LLDPE particles than for alumina particles. Similarly, when we compare glass and alumina particles at approximately the same excess gas velocity in Figures 11 and 12, we find that more bubbles are predicted for alumina. Generally speaking, particles with stronger energy dissipation characteristics are expected to show more vigorous fluidization and larger bubbles. In our case, this is especially apparent for LLDPE particles.

Bubble size

Literature correlations for the bubble size are usually given as a function of height and excess gas velocity. In this work, we compare the bubble size with correlations of Darton et al.[32] and Werther.[33] For the Darton et al. correlation the initial bubble size A_0 was set to zero, assuming zero bubble size at zero height. Figures 13–16 show the equivalent bubble diameter as function of height for different materials and different superficial gas velocities. In all cases, a monotonously increasing trend in the equivalent bubble diameter with height is observed, both experimentally and numerically. We find that at low superficial gas velocity (Figures 13 and 14) the experiments and simulations follow the

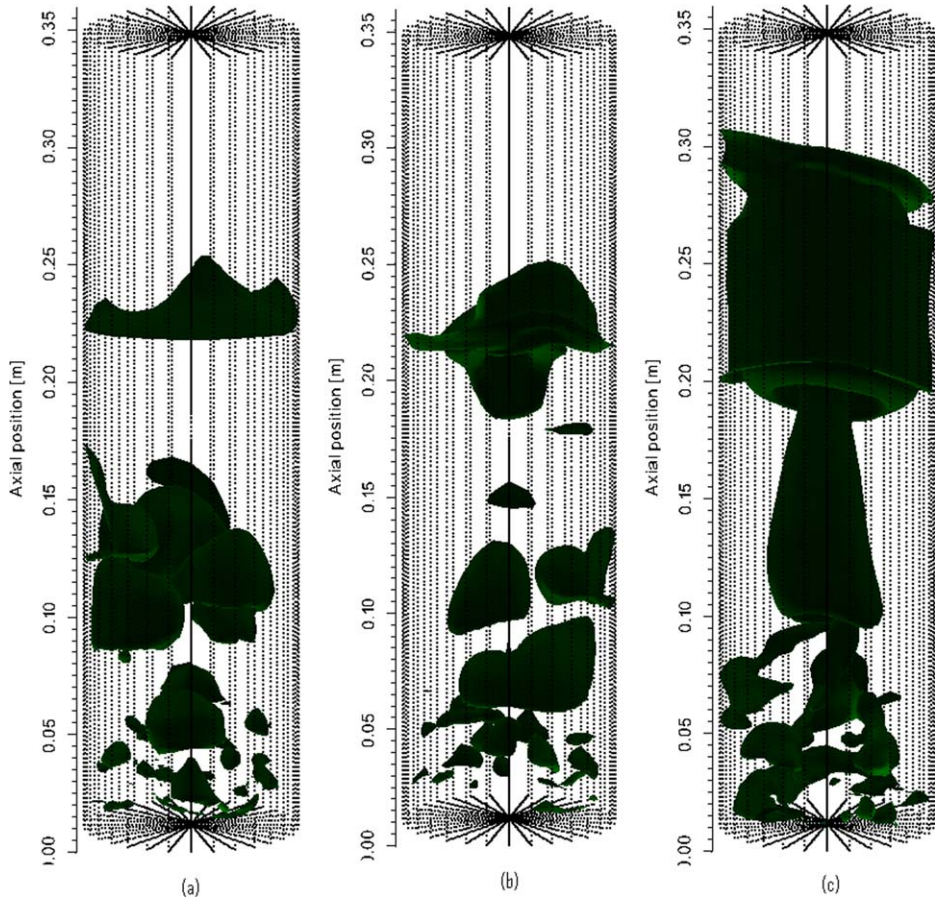

Figure 6. Snapshot of bubble contours obtained from simulations at time of 2.5 s after initiation of fluidization with an inlet gas velocity of 1.5 U_{mf} for (a) alumina, (b) LLDPE, and (c) glass.

[Color figure can be viewed in the online issue, which is available at wileyonlinelibrary.com.]

Darton correlation, whereas at high gas velocity (Figures 15 and 16) the trend shifts toward the Werther correlation. The Darton correlation does not take into account a mechanism of bubble splitting and breakage. Therefore, the size of an individual bubble shows a continuously increasing trend. Such a continuous development of bubble size is expected at low gas velocity, where the bubble does not achieve excessive growth. It is also known that Geldart B and D particles do not show pronounced breakage or splitting of bubbles.[5] However, when we compare the bubble size distributions in

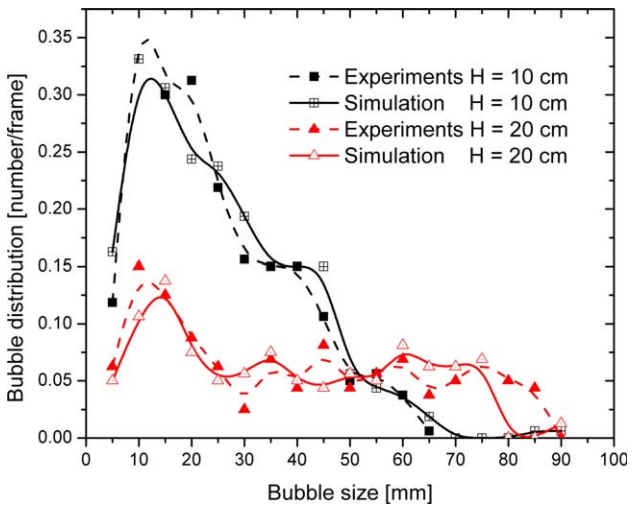

Figure 7. Bubble size distribution for LLDPE particles at inlet gas velocity of 1.5 U_{mf} at two heights.

[Color figure can be viewed in the online issue, which is available at wileyonlinelibrary.com.]

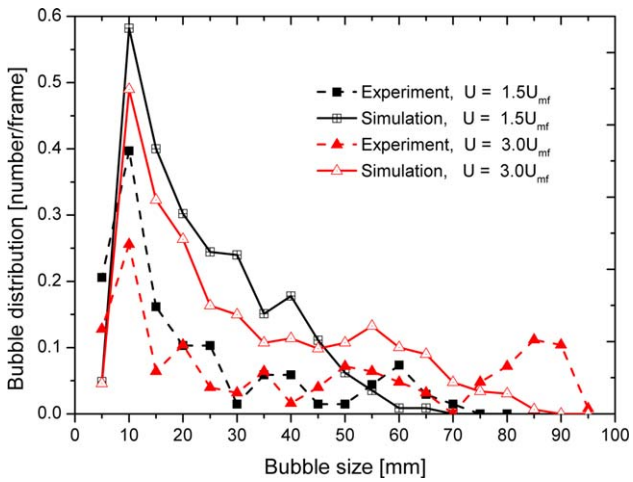

Figure 8. Bubble size distribution for alumina particles at a height of 10 cm from the bottom for two different inlet gas velocities.

[Color figure can be viewed in the online issue, which is available at wileyonlinelibrary.com.]

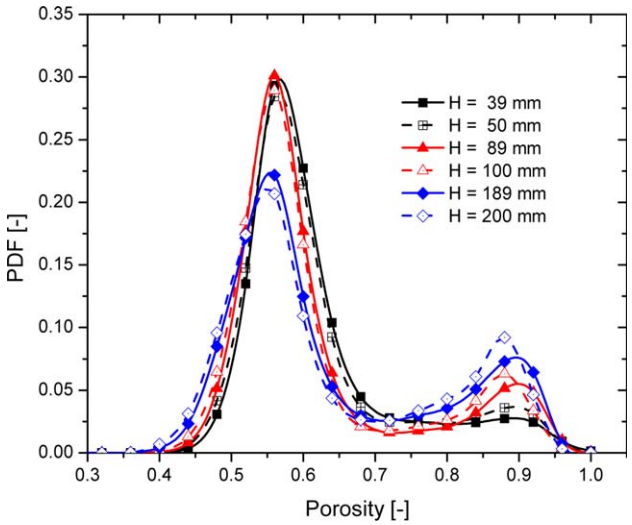

Figure 9. PDF for glass particles fluidizing at 2.0 U_{mf} at six heights obtained from three independent measurement series.

[Color figure can be viewed in the online issue, which is available at wileyonlinelibrary.com.]

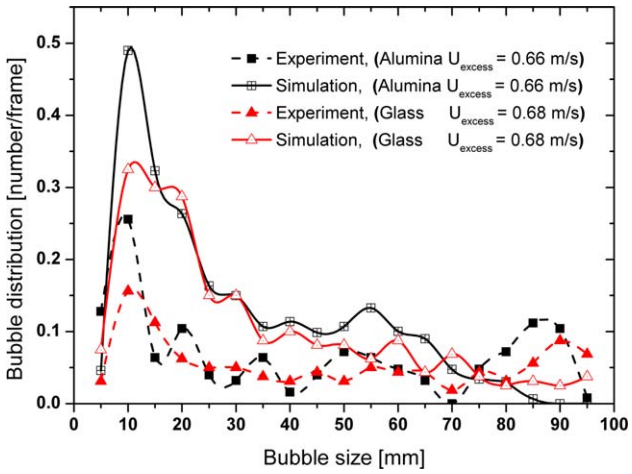

Figure 11. Bubble size distribution at a height of 10 cm from the bottom, comparing glass and alumina particles at approximately same excess gas velocities.

[Color figure can be viewed in the online issue, which is available at wileyonlinelibrary.com.]

Figures 7, 8, and 11, we find that a considerable number of small bubbles are observed at both high and low gas velocities, even in the top section of the bed. Occurrence of these smaller bubbles may be the result of breakage of larger bubbles. We also observed that this phenomenon is much more pronounced for the case of glass particles (see Figure 14 at the height of 20 cm) than for LLDPE and alumina (Figures 15 and 16). We conjecture that this is due to the difference in energy dissipation of different particles, where alumina and LLDPE exhibit more dissipation than glass. Also, note that the glass particles lie on the boundary between Geldart B and D classification, and are, therefore, expected to show grouping characteristics of B and D. The shift from the Darton correlation to the Werther correlation at very high gas velocities and higher heights may also be caused by the fact that the actual size of the bubble cannot be accurately estimated on the basis of measurements in a horizontal cross-sectional plane. Due to the finite size of our system (wall effect), larger bubbles prefer to get elongated. If a bubble is elongated in the vertical direction, the equivalent bubble diameter based on a cross-sectional analysis will be less than the actual equivalent bubble diameter.

Comparing experiments with simulation results on the bubble size, we observe that the experiments show larger bubbles. The same relative difference was observed for all measurements, irrespective of flow rate and/or measurement height. The experimental and simulation measurements, together with literature correlation are given in Figures 13–16, where the vertical bars represent standard deviations in the observed bubble size.

To find the reason for the observed difference between experiments and simulations, let us reconsider the bubble size distribution at a height of 10 cm inside the bed, where

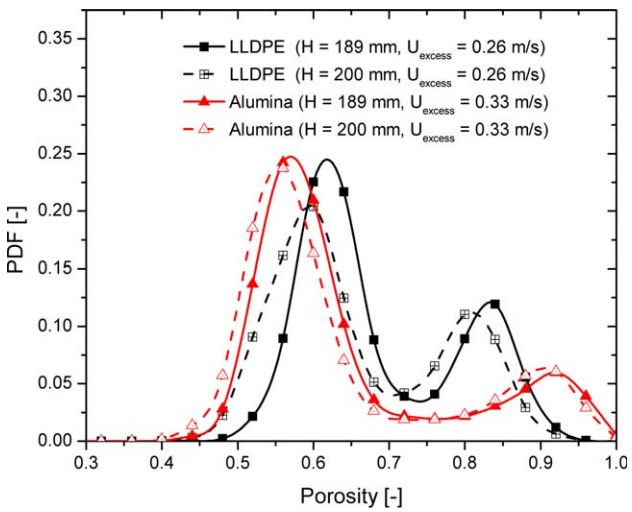

Figure 10. PDF plots from the experiments for LLDPE and alumina particles at 2.0 U_{mf}.

[Color figure can be viewed in the online issue, which is available at wileyonlinelibrary.com.]

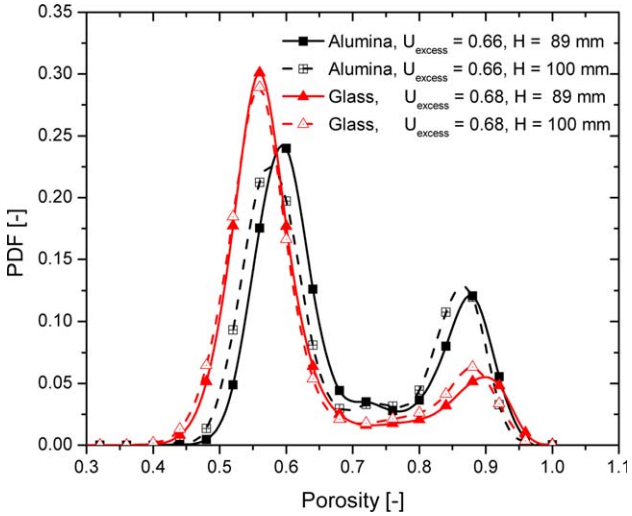

Figure 12. PDF plots from the experiments for alumina and glass particles at approximately same excess gas velocities.

[Color figure can be viewed in the online issue, which is available at wileyonlinelibrary.com.]

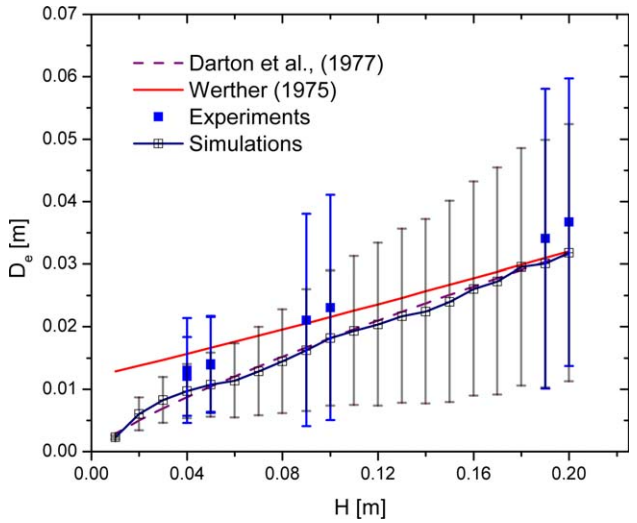

Figure 13. Equivalent bubble diameter as a function of height for LLDPE particles at inlet gas velocity of 1.25 U_{mf}.

Vertical bars represent standard deviations in the measured bubble sizes. [Color figure can be viewed in the online issue, which is available at wileyonlinelibrary.com.]

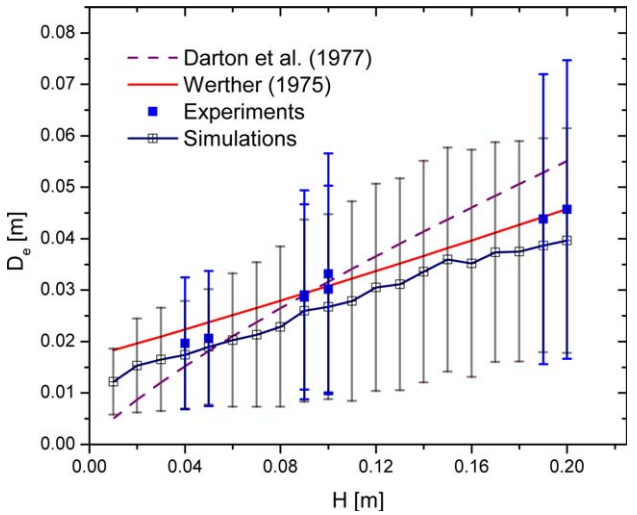

Figure 15. Equivalent bubble diameter as a function of height for LLDPE particles at inlet gas velocity of 2.0 U_{mf}.

Vertical bars represent standard deviations. [Color figure can be viewed in the online issue, which is available at wileyonlinelibrary.com.]

we do not expect much bubble breakage. We found that the simulations predict a larger fraction of smaller bubbles compared to experiments (Figures 8 and 11). One may speculate that the X-rays fail to detect smaller bubbles, or the experimental image processing does not detect smaller bubbles. We can exclude these explanations, because at low inlet gas velocities, where mainly small bubbles are formed, almost the same bubble size distribution is observed in both experiments and simulations, see Figure 7. To obtain a detailed understanding of the bubble size distribution at different gas flow rates, we have analyzed sequences of X-ray images with the intermediate image processing steps carried out for detecting bubbles in the images (in the experiments) and data (in the simulations). We found that even at high gas velocity, the X-ray images contain both small and large bubbles throughout the measured bed height. During the image processing, small bubbles are detected if they are alone in the cross-sectional plane or sufficiently far away from larger bubbles. However, if the small bubbles occur in the vicinity of larger bubbles, the small bubbles were not detected individually, but merged into the large bubbles during the edge detection step. On the contrary, in the simulation data processing this was not the case because the bubbles were detected based upon a fixed threshold value for the porosity, and smoothing of bubbles was performed using linear interpolation of the porosity in the neighboring cells. If the sharpening steps are excluded from the image and data processing, the continuously increasing trend of bubble size with height is changed into a fluctuating trend. Therefore, we prefer to show the results in the current format and

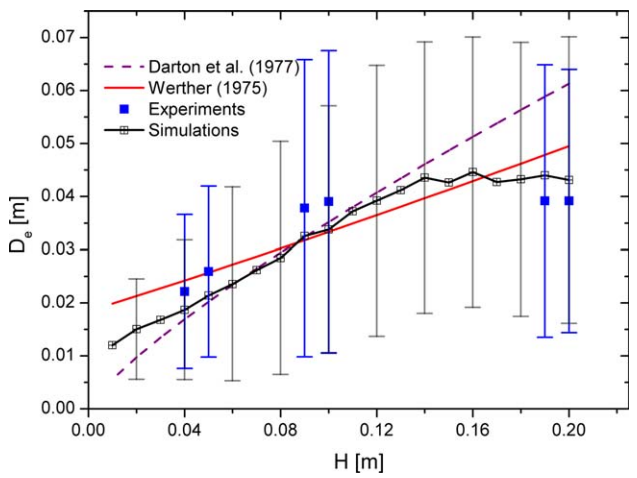

Figure 14. Equivalent bubble diameter as a function of height for glass particles at inlet gas velocity 1.5 U_{mf}.

Vertical bars represent standard deviations. [Color figure can be viewed in the online issue, which is available at wileyonlinelibrary.com.]

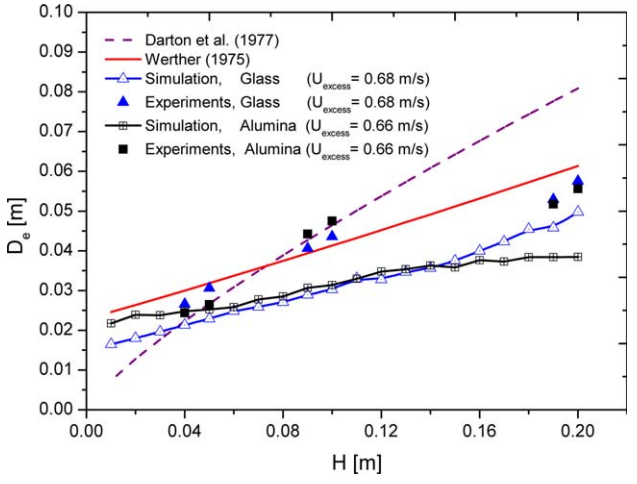

Figure 16. Equivalent bubble diameter as a function of height for glass and alumina particles, at approximately the same excess gas velocity.

[Color figure can be viewed in the online issue, which is available at wileyonlinelibrary.com.]

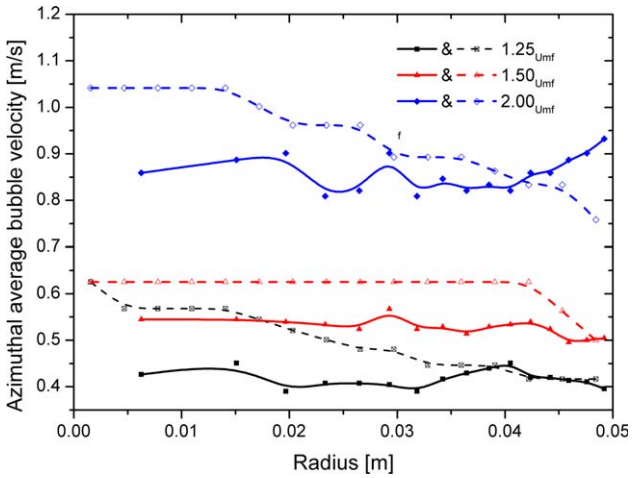

Figure 17. Azimuthally and time-average bubble rise velocity as a function of distance to the central axis for glass particles at a height of 10 cm from the bottom, comparing three different inlet gas velocities.

Solid lines represent experiments, dashed lines represent simulations. [Color figure can be viewed in the online issue, which is available at wileyonlinelibrary.com.]

attribute the difference between simulations and experiments to image processing of small bubbles.

Bubble velocity

We now focus on the bubble rise velocity. Figure 17 shows the average bubble rise velocity as a function of radial distance to the central axis, which has been azimuthally and time-averaged (as in Eq. 5, but averaged over a subset of the cells in a radial direction). The figure shows that there is no any significant change in bubble rise velocity with radial position. Therefore, from this point onward we investigate the cross-sectional average bubble rise velocity on a time-averaged scale.

Figure 18 shows the bubble rise velocity as a function of excess gas velocity for different materials at different heights. The bubble rise velocity increases with increasing excess gas velocity. The experimental measurement and simulation predictions are in good mutual agreement. The bubble rise velocity is in good agreement with the Hilligardt and Werther[34] correlation for glass and alumina particles. However, for LLDPE particles a higher bubble rise velocity was observed, most notably at the heights of 10 and 20 cm. The higher bubble rise velocity for LLDPE particles could be the result of a larger bubble size than predicted by the correlations. Although the bubble size as a function of height in Figures 13 and 15 shows consistency with the bubble size correlation of Werther,[33] this size is based on measurements in a horizontal cross-sectional plane, which

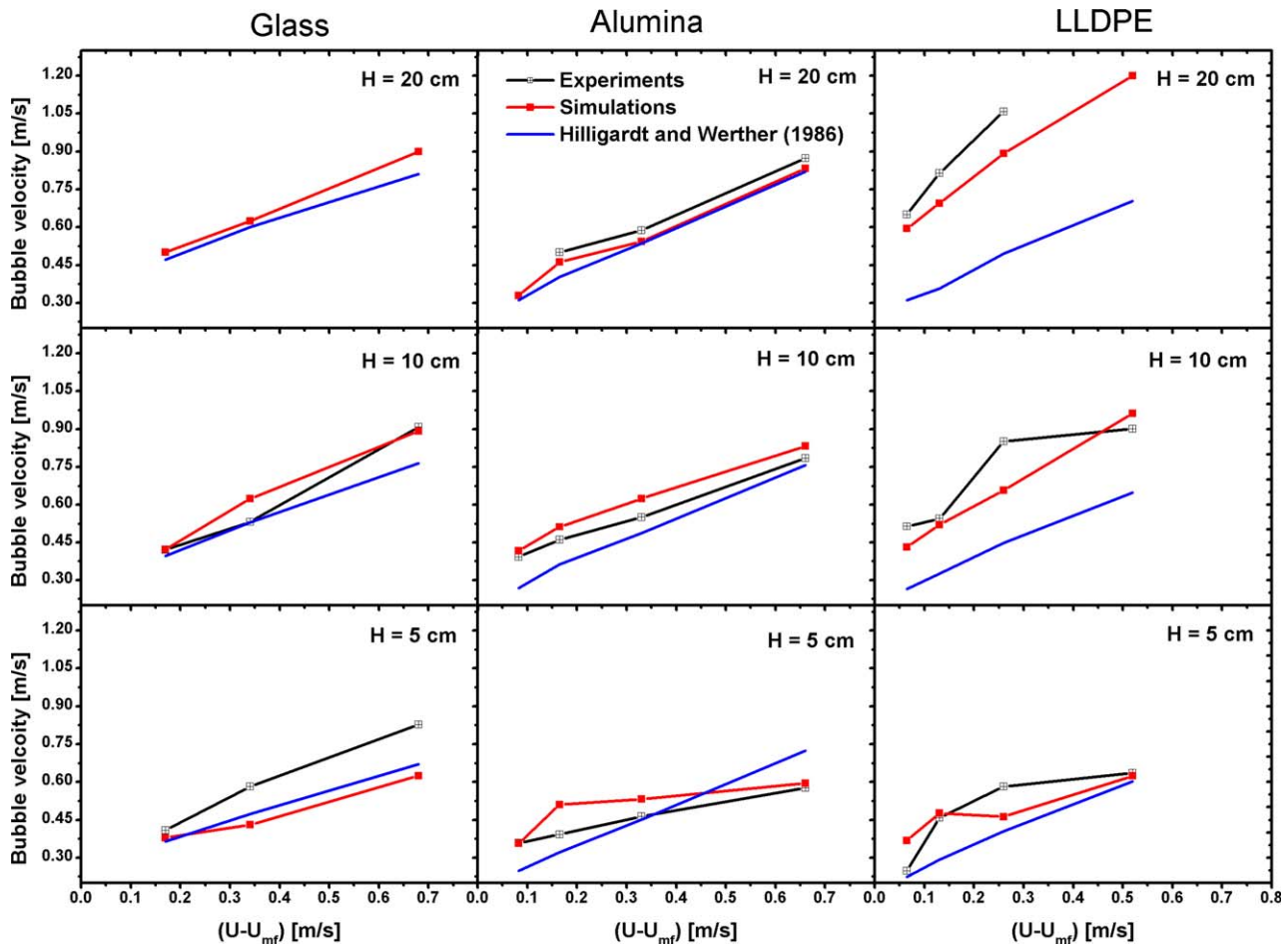

Figure 18. Bubble rise velocity as a function of excess gas velocity for different materials and different heights from the bottom.

Comparison between experiments, simulations and literature correlation. [Color figure can be viewed in the online issue, which is available at wileyonlinelibrary.com.]

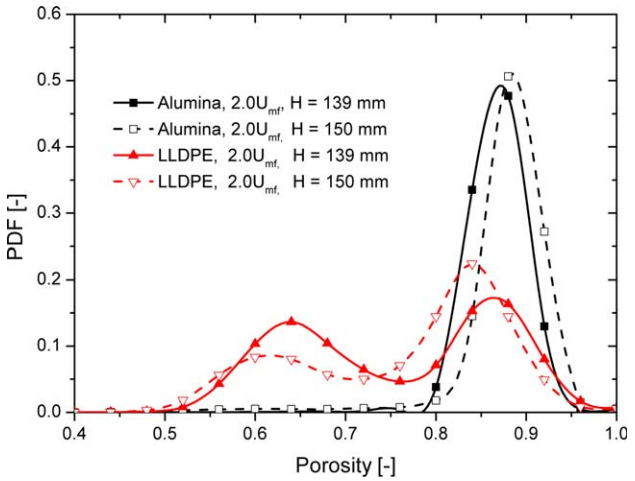

Figure 19. PDF plot for LLDPE and alumina particles at two heights in the freeboard region, for bed of aspect ratio AR = 1.

[Color figure can be viewed in the online issue, which is available at wileyonlinelibrary.com.]

ignores possible elongation of bubbles in the vertical direction, as we explained before. Furthermore, when we measure the PDF at 5 cm above the initial particle bed height (in the freeboard region) at 2.0 U_{mf} inlet gas velocity, we observe almost no emulsion phase in the case of alumina particles, as shown in Figure 19. However, in the case of LLDPE particles, almost equal fractions of emulsion phase and bubble phase are observed at this height, showing that the bed expansion is much higher for LLDPE particles. According to the PDF plot in Figure 10, this higher bed expansion could partly be explained by a higher net gas holdup for the highly inelastic LLDPE particles. This indicates that bubbles were rising much faster in an expanded emulsion phase. Similar very high bubble rise velocities were also observed by Godlieb et al.[9] at an operating pressure of 1 bar when they studied similar LLDPE particles in a 30-cm diameter bed. Therefore, we are convinced that the high bubble rise velocity is a true property of a FB of LLDPE particles. This could be caused by the lowered effective viscosity of the expanded emulsion phase.

Effect of aspect ratio of the bed

Three different initial particle bed heights were investigated, with a bed aspect ratio of 0.5, 1, and 2. No significant differences in bubble characteristics could be observed. This observation is consistent throughout the measurements, irrespective of the material and/or inlet gas velocity.

Conclusions

We investigated the bubble characteristics in a 3-D gas–solid FB using ultrafast electron beam X-ray tomography and compared them with numerical results from TFM simulations. We studied the effects of parameters such as bed material, inlet gas velocity, and initial particle bed height on the equivalent bubble diameter, the bubble rise velocity, bubble size distribution, and the porosity distribution. Very small bubbles in the vicinity of larger bubbles were difficult to detect from the tomographic images, leading to a significantly lower amount of small bubbles in the experiments compared to simulation predictions. As a consequence, the equivalent bubble diameter predicted from simulations is lower than experiments. Also, because the effective bubble diameter is calculated without taking into account the actual 3-D volume of the bubble, care should be taken when obtaining bubble diameters from horizontal cross-sections. These examples show that one should carefully choose the methodology to postprocess 3-D experiments and simulation data. The bubble rise velocities obtained from simulations are in reasonable agreement with experimental measurements. Our results on bubble rise velocity are in good agreement with the correlation of Hilligardt and Werther for the case of glass and alumina particles. For the case of LLDPE particles, the bubble rise velocity did not match with this correlation. The porosity distribution plot signifies that gas holdup is higher for LLDPE particles resulting in higher bed expansion and high bubble rise velocity. This shows that bubble characteristics depend highly upon the collisional properties of the particles. From our combined analysis on equivalent bubble size, PDF plots and porosity distribution plots, we find that the bubbles in LLDPE particles show unique behavior when compared with bubbles in glass and alumina particles. We can conclude that TFM simulations can be used to extract detailed insight in the bubbles and solids flow characteristics in 3-D FBs.

Acknowledgment

The authors thank the European Research Council for its financial support, under its Advanced Investigator Grant scheme, contract number 247298 (MultiscaleFlows).

Notation

C = fluctuation particle velocity, m/s
g = gravitational acceleration, m/s^2
I = unit tensor
p = pressure, Pa
q = kinetic fluctuation energy, kg/s
u = velocity, m/s
t = time, s
e_n = coefficient of restitution–
U_{mf} = minimum fluidization velocity, m/s
A_b = area of bubble, m^2
D_e = equivalent bubble diameter, m
H = height from the bottom/distributor, m

Greek letters

β = interphase momentum transfer coefficient, kg/m^3/s
γ = dissipation due to inelastic particles collisions, kg/m/s^3
ε = volume fraction–
ρ = density, kg/m^3
Θ = pseudo particle temperature, m^2/s^2
τ = stress tensor, Pa
μ = shear viscosity, kg/(m s)

Subscripts

s = solid phase
g = gas phase
p = particle
b = bubble
mf = minimum fluidization
e = equivalent
max = maximum
min = minimum

Literature Cited

1. Kunii D, Levenspiel O. *Fluidization Engineering*, *2nd ed.* Newton, MA: Butterworth-Heinemann, 1991.

2. Van Swaaij WPM. Chemical reactors. In: Davidson JF, Clift R, Harrison D, editors. *Fluidization*, *2nd ed*. London: Academic Press, 1985: 595–629.
3. Werther J. Measurement techniques in fluidized beds. *Powder Technol*. 1999;102:15–36.
4. Werther J, Molerus O. The local structure of gas fluidized beds-I. A statistically based measuring system. *Int J Multiphase Flow*. 1973;1: 103–122.
5. Karimipour S, Pugsley T. A critical evaluation of literature correlations for predicting bubble size and velocity in gas–solid fluidized beds. *Powder Technol*. 2011;205:1–14.
6. Rautenbach C, Mudde RF, Yang X, Melaaen MC, Halvorsen BM. A comparative study between electrical capacitance tomography and time-resolved X-ray tomography. *Flow Meas Instrum*. 2013;30:34–44.
7. Makkawi Y, Wright P. Electrical capacitance tomography for conventional fluidized bed measurements-remarks on the measuring technique. *Powder Technol*. 2004;148:142–157.
8. Mudde RF. Time-resolved X-ray tomography of a fluidized bed. *Powder Technol*. 2010;199:55–59.
9. Godlieb W, Gorter S, Deen NG, Kuipers JAM. Experimental study of large scale fluidized beds at elevated pressure. *Ind Eng Chem Res*. 2012;51:1962–1969.
10. Hulme I, Kantzas A. Determination of bubble diameter and axial velocity for a polyethylene fluidized bed using X-ray fluoroscopy. *Powder Technol*. 2004;147:20–33.
11. Bieberle M, Barthel F, Hampel U. Ultrafast X-ray computed tomography for the analysis of gas–solid fluidized beds. *Chem Eng J*. 2012;189–190:356–363.
12. Brouwer GC, Wagner EC, van Ommen JR, Mudde RF. Effects of pressure and fines content on bubble diameter in a fluidized bed studied using fast X-ray tomography. *Chem Eng J*. 2012;207–208: 711–717.
13. Fischer F, Hoppe D, Schleicher E, Mattausch G, Flaske H, Bartel R, Hampel U. An ultra-fast electron beam X-ray tomography scanner. *Meas Sci Technol*. 2008;19:094002.
14. Bieberle M, Schleicher E, Fischer F, Koch D, Menz H-J, Mayer H-G, Hampel U. Dual-plane ultrafast limited-angle electron beam X-ray tomography. *Flow Meas Instrum*. 2010;21(3):233–239.
15. Goldschmidt MJV, Beetstra R, Kuipers JAM. Hydrodynamic modelling of dense gas-fluidised beds: comparison and validation of 3D discrete particle and continuum models. *Powder Technol*. 2004;142: 23–47.
16. Wang Y, Chao Z, Jakobsen HA. A sensitivity study of the two-fluid model closure parameters determining the main gas–solid flow pattern characteristics. *Ind Eng Chem Res*. 2010;49:3433–3444.
17. Lindborg H, Lysberg M, Jakobsen HA. Practical validation of the two-fluid model applied to dense gas-solid flow in fluidized beds. *Chem Eng Sci*. 2007;62:5854–5869.
18. Cammarata L, Lettieri P, Micale G, Colman D. 2D and 3D CFD simulations of bubbling fluidized beds using Eulerian–Eulerian models. *Int J Chem React Eng*. 2003;1(A48):1–19.
19. Hansen KG, Solberg T, Hjertager BH. A three-dimensional simulation of gas/particle flow and ozone decomposition in the riser of a circulating fluidized bed. *Chem Eng Sci*. 2004;59:5217–5224.
20. Lindborg H, Lysberg M, Jakobsen HA. Practical validation of the two-fluid model applied to dense gas-solid flow in fluidized beds. *Chem Eng Sci*. 2007;62:5854–5869.
21. Geldart D. The size and frequency of bubble in two and three dimensional gas-solid fluidized beds. *Powder Technol*. 1970;4:41.
22. Chandrasekaran BK, van der Lee L, Hulme I, Kantzas A. A simulation and experimental study of the hydrodynamic of bubbling fludized bed of linear low density polyethylene using bubble properties and pressure fluctuations. *Macromol Mater Eng*. 2005;290:592–608.
23. Verma V, Deen NG, Padding JT, Kuipers JAM. Two-fluid modeling of three-dimensional cylindrical gas–solid fluidized beds using the kinetic theory of granular flow. *Chem Eng Sci*. 2013;102:227–245.
24. Fischern F, Hampel U. Ultra fast electron beam X-ray computed tomography for two-phase flow measurement. *Nucl Eng Des*. 2010; 240:2254–2259.
25. Ding J, Gidaspow D. A bubbling fluidization model using kinetic theory of granular flow. *AIChE J*. 1990;36:523–538.
26. Kuipers JAM, van Duin KJ, van Beckum FPH, van Swaaij WPM. A numerical model of gas-fluidized beds. *Chem Eng Sci*. 1992;47: 1913–1924.
27. Gidaspow D. Multiphase flow and fluidization: continuum and kinetic theory descriptions. Boston: Academic Press, 1994.
28. Nieuwland JJ. Hydrodynamic modelling of gas-solid two-phase flows. Ph.D. Thesis. Enschede, The Netherlands: Twente University, 1995.
29. van der Hoef MA, Beetstra R, Kuipers JAM. Lattice-Boltzmann simulations of low-Reynolds number flow past mono- and bidisperse arrays of spheres: results for the permeability and drag force. *J Fluid Mech*. 2005;528:233–254.
30. Srivastava A, Sundaresan S. Analysis of a frictional-kinetic model for gas-particle flow. *Powder Technol*. 2003;129:72–85.
31. Otsu N. A threshold selection method from grey-level histogram. *IEEE Trans Syst Man Cybern*. 1979;9:62–66.
32. Darton RC, La Naueza RD, Davidson JF, Harrison D. Bubble growth due to coalescence in fluidized beds. *Trans Inst Chem Eng*. 1977;55:274–280.
33. Werther J. Bubble growth in a large diameter fluidized beds, International Fluidization Conference, Pacific Grove, USA, 1975. In: Keairns DL editor. *Fluidization Technology*. Washington DC: Hemisphere Publication Co., 1976: 215–235.
34. Hilligardt K, Werther J. Local bubble gas hold-up and expansion of gas/solid fluidized beds. *Ger Chem Eng*. 1986;9:215–221.
35. Davidson JF, Harrison D, Darton RC, LaNauze RD. The two-phase theory of fluidization and its application to chemical reactors. In: Lapidus L, Arnundson NR, editors. *Chemical Reactor Theory: A Review*. New York: Prentice-Hall, 1977:583.
36. Toomey RD, Johnstone HF. Gaseous fluidization of solid particles. *Chem Eng Prog*. 1952;48:220–225.

Manuscript received Sept. 27, 2014, and final revision received Jan. 28, 2014.